

Dual-Species Synchronous Spin-Exchange Optical Pumping

D. A. Thrasher, S. S. Sorensen, and T. G. Walker*

Department of Physics, University of Wisconsin-Madison, Madison, Wisconsin 53706, USA

(Dated: December 12, 2019)

We demonstrate a novel quantum sensor for measuring non-magnetic spin-dependent interactions. This sensor utilizes ^{131}Xe , ^{129}Xe , and ^{85}Rb which are continuously polarized transverse to a pulsed bias field. The transverse geometry of this spin-exchange pumped comagnetometer suppresses longitudinal polarization, which is an important source of systematic error. Simultaneous excitation of both Xe isotopes is accomplished by frequency modulating the repetition rate of the bias field pulses at subharmonics of the Xe Larmor resonance frequencies. The area of each bias pulse causes 2π Larmor precession of the Rb. We present continuous dual-species Xe excitation and discuss a temperature-dependent wall interaction that limits the ^{129}Xe polarization. The Rb atoms serve as an embedded magnetometer for detection of the Xe precession. We discuss Rb magnetometer phase shifts, and show that even first-order treatments of these phase shifts can result in order-of-magnitude improvements in the achieved field suppression when performing comagnetometry. The sensing bandwidth of the presented device is 1 Hz, and we demonstrate a white-noise level of $7 \mu\text{Hz}/\sqrt{\text{Hz}}$ and a bias instability of $\sim 1 \mu\text{Hz}$.

I. INTRODUCTION

Spin-exchange (SE) pumped comagnetometers [1, 2] enable precise sensing of spin-dependent phenomena with benchtop-scale experiments. Such devices have found broad use in the precision measurement community, with applications ranging from measuring inertial rotation [2–5] to placing upper bounds on spin-mass couplings [6, 7], Lorentz violations [8–12], and atomic electric dipole moments [13–15].

The potential for miniaturization has made gyroscope implementations a subject of interest in industrial research [2, 16, 17]. Indeed, advances in chip-scale technologies have opened the door for SE pumped comagnetometers whose performance is predicted to scale favorably with the size of the sensor compared to alternative devices such as ring laser gyroscopes [18]. Practical inertial navigation devices must provide continuous readout. The device presented in this work was designed to suppress systematic errors from longitudinal polarization while satisfying the constraint of continuous operation.

SE pumped comagnetometers consist of co-located ensembles of noble gas nuclei and alkali-metal atoms which are spin polarized in the presence of a magnetic field [19]. Suppose an ensemble of two spin-exchange optically pumped (SEOP) noble gas species (a and b) are each subject to a common magnetic field B_z and some spin-dependent interaction X . The Larmor resonance frequency of each isotope obeys [2, 20–22]

$$\Omega^a = \gamma^a (B_z + b_S^a S_z + b_K^a K_z) + X_z^a, \quad (1a)$$

$$\Omega^b = \gamma^b (B_z + b_S^b S_z + b_K^b K_z) + X_z^b, \quad (1b)$$

where γ is the gyromagnetic ratio, S and K are the respective alkali-metal and noble gas polarizations, z sub-

scripts refer to the longitudinal components (*i.e.*, parallel to the bias field direction), and b_j^i is the SE coefficient [23] characterizing the influence of j 's polarization on i . Given a known $\rho = \gamma^a/\gamma^b$, Ω^a and Ω^b can be simultaneously measured in order to suppress B_z while retaining sensitivity to X_z^a and X_z^b [24]. The longitudinal polarizations S_z and K_z are important sources of systematic error in SE pumped comagnetometers [6, 20, 21].

The embedded alkali-metal atoms can be used for quantum non-demolition readout [25, 26] of the noble gas precession. During atomic collisions, a Fermi-contact interaction enhances the field experienced by the alkali-metal atoms due to the the polarized noble gas nuclei [27]. This enhancement factor directly improves the signal-to-noise-ratio (SNR) as classical fields are not similarly enhanced. Using the alkali-metal atoms also enables miniaturization by eliminating the need for an exterior pick-up coil (such as a SQUID [14, 15]).

The device demonstrated in this work is a SE pumped ^{131}Xe - ^{129}Xe comagnetometer which produces no first-order time-averaged S_z or K_z such that the comagnetometer signal

$$\xi \equiv \frac{\rho\Omega^b - \Omega^a}{1 + \rho} \approx \frac{\rho X_z^b - X_z^a}{1 + \rho} \quad (2)$$

is independent of magnetic fields, where the superscripts a and b refer to ^{129}Xe and ^{131}Xe , respectively, and $\rho = 3.373417(38)$ [28]. In the context of rotation sensing, we set $X_z^b = \omega^R$ and $X_z^a = -\omega^R$ [2] such that ξ becomes the rotation frequency ω^R . The noble gas nuclei are continuously polarized perpendicular to a frequency-modulated pulsed bias field, utilizing a dual-species extension of synchronous SEOP [29, 30]. We demonstrate that the ^{131}Xe and ^{129}Xe Larmor precession frequencies are sufficiently correlated to resolve a white frequency noise level of $7 \mu\text{Hz}/\sqrt{\text{Hz}}$ and achieve a low-frequency field noise suppression in excess of 10^3 . The scale factor between the Larmor resonance frequencies and the spin-dependent interactions is determined predominantly by fundamental

* tgwalker@wisc.edu

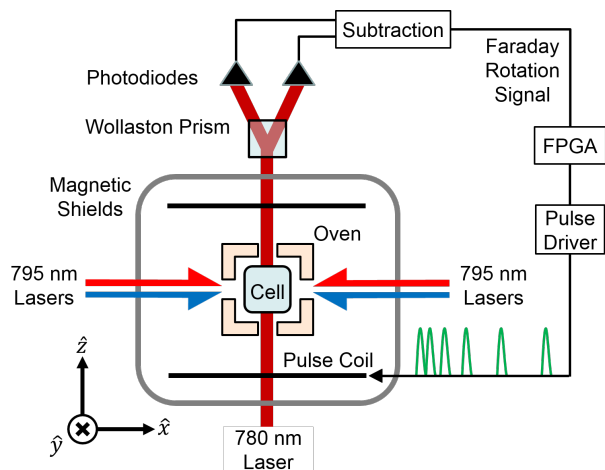


FIG. 1: Schematic of apparatus. Field shim coils are not shown. The green trace depicts the frequency modulated bias field pulses.

physical constants, namely the gyromagnetic ratios. It is, to a good approximation [31], independent of the details of our apparatus (such as temperature, gas pressures, etc.). This means that comagnetometry can be performed without the need for calibration.

Figure 1 shows a schematic of the experimental apparatus. We optically pump ^{85}Rb atoms along \hat{x} , and noble gas nuclei are polarized via SE collisions with the polarized Rb atoms. The bias field is oriented along \hat{z} (transverse to the Rb polarization) and is applied as a series of low-duty-cycle pulses. The pulse area is set such that the Rb spins precess 2π radians during each bias pulse. The Xe isotopes precess only $\sim 2\pi/10^3$ radians per pulse (owing to their much smaller magnetic moments). As such, we can approximate the effective bias field experienced by the Xe isotopes due to the pulses as a continuous function,

$$B_p(t) = \omega_p(t)/\gamma^S, \quad (3)$$

where $\omega_p(t)$ is the repetition rate of the 2π pulses and $\hbar\gamma^S = 2\mu_B/(2I+1)$, where $I = 5/2$ is the ^{85}Rb nuclear spin and μ_B is the Bohr magneton. The repetition rate of the bias field pulses is modulated at linear combinations of Ω^a and Ω^b in order to simultaneously excite the magnetic resonance of both noble gas species.

Continuous detection of the noble gas precession is accomplished using the embedded Rb magnetometer, which is effectively at zero-field due to the bias field being applied as low-duty-cycle 2π pulses [32]. We monitor $S_z \propto K_y$ by measuring the Faraday rotation of a linearly polarized probe laser which propagates along \hat{z} (parallel to the bias field). We demodulate the S_z signal digitally using an FPGA. Resonance for each Xe species is maintained by adjusting the modulation frequencies of the pulsed bias field repetition rate, and ξ is computed using the Xe resonance frequencies determined by this feedback.

This paper expands on the work presented in Ref. [30] and proceeds as follows. Section II describes the simultaneous excitation, detection, and demodulation of ^{131}Xe and ^{129}Xe precession. We give details of the experimental apparatus and demonstrate dual-species Xe excitation. In Sec. III, we perform comagnetometry and present the field suppression and stability of the system. Section IV provides an outlook for possible future studies, and we conclude in Sec. V with a summary of the presented work.

II. EXCITATION AND DETECTION

A. Principles

We assume purely transverse optical pumping of the Rb along \hat{x} . We also assume that transverse fields experienced by the Xe, including the SE field $b_S^K S_x$, are well-nulled, such that the longitudinal components of the Xe polarizations are negligible [29].

The transverse components $K_+ = K_x + iK_y$ of the nuclear spin polarization for each noble gas species obey

$$\frac{dK_+}{dt} = -(\mp i\Omega + \Gamma_2)K_+ + \Gamma_S^K S_+ \quad (4)$$

where $\Omega = \gamma B_z + X_z$ is the Larmor resonance frequency, arising from both magnetic field B_z and spin-dependent phenomena X_z . The SE rate constant is Γ_S^K , and the transverse relaxation rate is Γ_2 . The precession direction is encoded in the sign in front of Ω (top is ^{129}Xe , bottom is ^{131}Xe). The frequency shift of the ^{131}Xe due to quadrupole interactions is assumed to be independent of B_z . Such quadrupole effects are included in X_z^b .

Simultaneous excitation of multiple noble gas species via SE collisions with the Rb can be accomplished by modulating either S_+ or B_z . Previously we demonstrated single-species excitation by modulating S_+ [29]. While an extension of that approach is possible, here we perform dual-species excitation by modulating B_z . In this work, we modulate B_z by modulating the pulse repetition rate ω_p . This is advantageous because changes in ω_p impact the Rb magnetometer gain far less than do changes in DC fields.

The \hat{z} component of the magnetic field is $B_z = B_{z0} + B_p(t)$, which includes the stray field B_{z0} and the bias field from the 2π pulses $B_p(t) = B_{p0} + B_m(t)$, where B_m is the modulated part of the pulsed field. The Xe nuclei experience both B_{z0} and B_p , but because the Rb atoms precess by 2π during each bias pulse, the Rb atoms experience predominantly B_{z0} .

We find that the Rb magnetometer gain depends on the pulse repetition rate. We attribute this to changes in the effective relaxation rate of the magnetometer as the pulse repetition rate (and hence duty cycle) is varied [32]. Though the bias field is zero most of the time, any SE collisions that occur during a bias pulse will contribute to relaxation. Hence, the magnetometer gain will

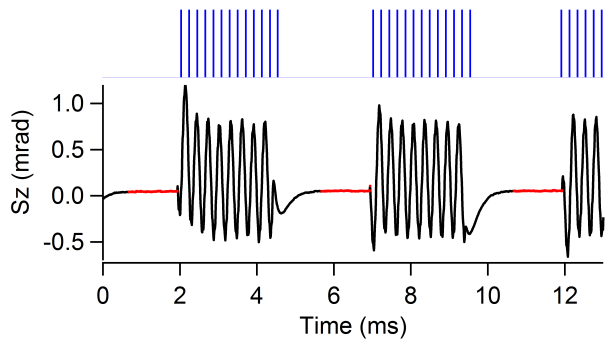


FIG. 2: Influence of bias pulse gating on Rb magnetometry. (Top) Time dependence of the few percent duty cycle bias pulses. (Bottom) Measured time dependence of raw S_z signal from polarimeter. Red data are averaged together to measure the Xe precession at an effective sampling rate of ω_3 . The $\approx 3\text{kHz}$ oscillation present when pulsing comes from interference between the AC heater drive and the pulses.

be increasingly degraded as pulses are applied more frequently. For the ω_p modulation presented in this work, the observed magnetometer gain varied up to a factor of two.

We suppress the influence of gain modulation on the detection by gating the 2π pulses. After the pulses are gated off, we wait for the magnetometer gain to recover before recording the Faraday signal (see Fig. 2). If we do not gate the pulses, we see a background on the recorded Faraday signal which corresponds to harmonics of the pulsing modulation frequencies. We find that waiting twice the $1/e$ recovery time of the Rb magnetometer before recording the Faraday signal suppresses this background. We modulate the 2π pulse repetition rate (depicted in Fig. 3) as

$$\omega_p(t) = \omega_{p0}g(t)(1 + b_1 \cos(\omega_1 t) + b_2 \cos(\omega_2 t)), \quad (5)$$

where $g(t) = (\text{sign}(\cos(\omega_3 t)) + 1)$ is the time dependence of the gating, $\omega_1 = \omega_d^b$ and $\omega_2 = \omega_d^a - 3\omega_d^b$ determine the Xe drive frequencies, and b_1 and b_2 set the depth of modulation.

1. Influence of Rb on drive, detection

The Rb atoms serve two primary purposes in our system: we use the DC transversely polarized Rb S_+ to polarize the Xe nuclei and the AC longitudinally polarized Rb S_z to detect the Xe precession. For $\Omega \ll \Gamma'$ the time-average solution to the Bloch equations for the Rb polarization

$$\mathbf{S} = \frac{\mathbf{R}\Gamma' + \boldsymbol{\Omega} \times \mathbf{R} + \boldsymbol{\Omega}(\boldsymbol{\Omega} \cdot \mathbf{R})/\Gamma'}{\Gamma'^2 + \boldsymbol{\Omega}^2} \quad (6)$$

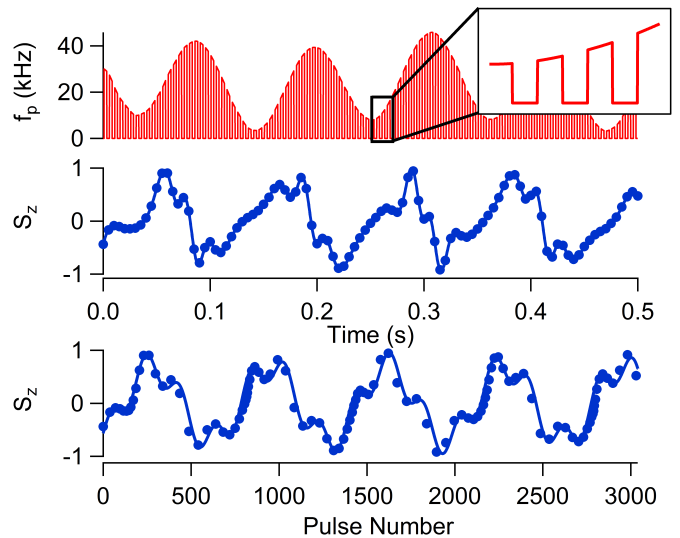


FIG. 3: Time dependence of bias pulse repetition rate (top) and normalized S_z sampled at ω_3 (middle) for $\Delta^a = \Delta^b = 0$. Corresponding pulse number dependence of normalized S_z (bottom). Filled circles are measured data. Lines are theory fits to the data. Inset depicts gating of the bias pulses.

can be expanded as

$$\mathbf{S} = \frac{\mathbf{R}}{\Gamma'} + \frac{\boldsymbol{\Omega} \times \mathbf{R}}{\Gamma'^2} + \frac{\boldsymbol{\Omega} \times \boldsymbol{\Omega} \times \mathbf{R}}{\Gamma'^3} + \dots, \quad (7)$$

where \mathbf{R} is the pumping rate, Γ' is the total relaxation rate (including pumping), and $\boldsymbol{\Omega} = \gamma^S \mathbf{B}$ where \mathbf{B} is the magnetic field experienced by the Rb. This assumes negligible back polarization from the Xe to the Rb [1, 33], and that \mathbf{K} precesses slowly such that S_z responds adiabatically. Since we optically pump along \hat{x} we have $\mathbf{R} = R\hat{x}$, and

$$S_+ = \frac{R}{\Gamma'} + i \frac{R\Omega_z}{\Gamma'^2} = \frac{R}{\Gamma'} e^{i\epsilon_z}, \quad (8a)$$

$$S_z = -\frac{R}{\Gamma'^2} (\Omega_y - \frac{\Omega_z}{\Gamma'} \Omega_x) = \frac{-R}{\Gamma'^2} \text{Im}[\gamma^S b_K^S K_+ e^{-i\epsilon_z}], \quad (8b)$$

where

$$\epsilon_z = \tan^{-1}\left(\frac{S_y}{S_x}\right) \equiv \tan^{-1}\left(\frac{B_{z0}}{B_w}\right) \ll 1 \quad (9)$$

is the magnetometer phase shift. $B_w = \Gamma'/\gamma^S$ is the magnetic width of the magnetometer. We see that though the Rb atoms are optically pumped along \hat{x} , the field B_{z0} causes the Rb polarization to rotate slightly into \hat{y} so that the transverse spin is phase shifted. We will show that this phase shift appears on the detected phase of rotating transverse fields (see Eq. 16) and must be accounted for in order to achieve optimal field suppression in the comagnetometer signal (see Sec. III A).

2. Magnitude and phase of K_+

We write the nuclear spin polarization using a phasor representation $K_+ = K_\perp e^{\pm i\phi}$. We measure the difference $\delta = \phi - \alpha$ between the instantaneous Xe phase ϕ and a reference phase $\alpha = \int (\omega_d + \gamma B_m) dt$ which is the phase the Xe would have if the only fields present were the pulsing fields and if $\Delta \equiv \omega_d - \Omega_0 = 0$ with $\Omega_0 = \gamma(B_{z0} + B_{p0}) + X_z$. To first order in δ and ϵ_z , the real part of Eq. 4 is

$$\frac{dK_\perp}{dt} = -\Gamma_2 K_\perp + \Gamma_S^K S_\perp [\cos(\alpha) - (\delta \mp \epsilon_z) \sin(\alpha)]. \quad (10)$$

To find the time averages of $\cos(\alpha)$ and $\sin(\alpha)$ (and thereby arrive at a steady-state solution for K_\perp), consider the time average of $e^{i\alpha}$ for $B_m = B_1 \cos(\omega_1 t) + B_2 \cos(\omega_2 t)$. Making substitutions using the Jacobi-Anger expansion

$$e^{iz \sin \theta} = \sum_{n=-\infty}^{\infty} J_n(z) e^{in\theta}, \quad (11)$$

where $J_n(z)$ is the n -th Bessel function of the first kind, and keeping only terms of the sums that would mix to give a contribution at DC, we find the time averages $\cos(\alpha) = J_{-p}(\frac{\gamma B_1}{\omega_1}) J_{-q}(\frac{\gamma B_2}{\omega_2})$ and $\sin(\alpha) = 0$. The steady-state solution for K_\perp is then

$$K_\perp = \frac{\Gamma_S^K S_\perp}{\Gamma_2} J_{-p}\left(\frac{\gamma B_1}{\omega_1}\right) J_{-q}\left(\frac{\gamma B_2}{\omega_2}\right) \quad (12)$$

with $p = 3$, $q = 1$ for ^{129}Xe and $p = 1$, $q = 0$ for ^{131}Xe chosen to satisfy the resonance condition $\omega_d = p\omega_1 + q\omega_2$.

The imaginary part of Eq. 4 is

$$\frac{d\phi}{dt} = \Omega - \frac{\Gamma_S^K S_\perp}{K_\perp} \sin(\phi \mp \epsilon_z). \quad (13)$$

To get an expression for δ , we make substitutions as given above and use the steady-state solution for K_\perp . To first order in δ and ϵ_z , we arrive at

$$\frac{d\delta}{dt} = -\Delta - \Gamma_2 (\delta \mp \epsilon_z). \quad (14)$$

The sign in front of ϵ_z is isotope dependent because the Xe isotopes precess in opposite directions.

3. Detection and demodulation

From Eq. 8 and Eq. 12, the magnetometer signal S_z can be written as

$$S_z = A_1^a \sin(\delta^a + \alpha^a - \epsilon_z) + A_1^b \sin(\delta^b + \alpha^b + \epsilon_z), \quad (15)$$

where $A_1 = -\gamma^S b_K^S K_\perp R / \Gamma'^2$. Note that the Rb precession phase includes both the Xe precession phase and the magnetometer phase shift.

The precession phase of each isotope can be extracted from S_z by demodulation with $\cos(\alpha)$. For example,

$$\begin{aligned} \int d\alpha^b S_z \cos(\alpha^b) &= \int dt \frac{d\alpha^b}{dt} S_z \cos(\alpha^b) \\ &= A_1^b \sin(\delta^b + \epsilon_z) + res. \end{aligned} \quad (16)$$

We sample evenly in time for experimental convenience, necessitating the $\frac{d\alpha}{dt}$ in the demodulation. Note the orthogonality between $\frac{d\alpha^a}{dt} \cos(\alpha^a)$ and $\frac{d\alpha^b}{dt} \cos(\alpha^b)$ which prevents isotope a 's phase information from showing up on isotope b 's detection channel and vice versa. The S_z signal is sampled at ω_3 and then low-pass filtered to prevent aliasing. The time average is approximated using a moving average over N data points, where N is chosen to suppress the high frequency residuals of the demodulation.

B. Apparatus

The experimental apparatus is similar to that described previously in Ref. [29]. An 8 mm cubic Pyrex cell filled with 40 Torr enriched Xe and 50 Torr N_2 with a hydride coating [17] is mounted in a ceramic housing which is secured inside a 3D-printed magnetic field coil rig, which is itself mounted in a three-layer cylindrical mu-metal shield (see Fig. 1). The coil rig consists of three square orthogonal Helmholtz coils (for nulling stray fields) and a multipole pulsing coil designed specifically to have low inductance, high field uniformity across the cell, and low magnetic moment (to reduce coupling to the shield endcaps). The multipole pulsing coil consists of two pairs of square coils wound in series with opposite polarity. The circuit used to drive the pulsing coil was custom-made using a modified H-bridge design. The bias field requires short pulses ($< 5 \mu\text{sec}$) of ≈ 1 Ampere peak current. To facilitate modulated- ω_p operation, the circuit was designed such that the Rb Larmor precession produced by each pulse is largely independent of the pulse repetition rate. The cell is heated to $\sim 120^\circ\text{C}$ by applying AC current at ~ 150 kHz to four pairs of heater coils printed on each face of the cell's ceramic housing.

To perform optical pumping of the Rb, the outputs of two distributed feedback laser diodes tuned near the Rb D1 transition (one on either side of resonance) are overlapped. The resulting beam is then split and circularly polarized so that half of each laser's power is directed to the cell from opposing directions ($\pm \hat{x}$), thereby reducing intensity gradients. The total pump light incident to the cell is nominally 30 mW. The power and detuning of each pump laser is chosen to null the average AC Stark field seen by the Rb. The average pump detuning is ≈ 12 GHz.

To detect S_z , approximately one mW of linearly polarized light from the output of a third distributed feedback laser diode, tuned near the Rb D2 line, is directed through the center of the cell and parallel to \hat{z} . Its polarization is analyzed via a balanced polarimeter. An FPGA synced to a commercial Rb time standard is used to synthesize the 2π pulse triggers, demodulate the digitized Faraday rotation signal, and perform feedback to correct the pulse repetition rate modulation frequencies so that the measured phase of each Xe isotope is kept equal to zero.

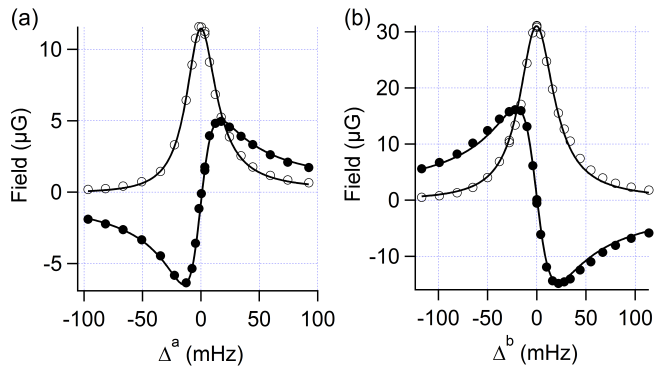


FIG. 4: Xe NMR Lineshapes. (a) $b_a^S K_1^a$ vs Δ^a . (b) $b_b^S K_1^b$ vs Δ^b . Filled circles are measured data. Lines are Lorentzian fits to the data.

C. Xe signals

The demodulated S_z vs. δ for each isotope is shown in Fig. 4. The data were acquired with one isotope driven on resonance while the other isotope's detuning was varied. The field modulation parameters were, $\omega_3 = 2\pi \times 200$ Hz, $b_1 = 0.73$ and $b_2 = 0.15$, and $\omega_{p0} \approx 2\pi \times 13.2$ kHz, resulting in average precession frequencies of ≈ 33.3 Hz and ≈ 9.9 Hz for ^{129}Xe and ^{131}Xe , respectively. Under these conditions, the amplitude of B_m was approximately $10B_w$. Only the modulation of 2π pulses allows for the Xe to experience such a large modulation while preserving the fidelity of the Rb magnetometer. The modulation parameters b_1 and b_2 were chosen to optimize the simultaneous excitation of both Xe species. Limiting $b_1 + b_2 < 1$ avoids producing Xe precessions near the $1/f$ detection noise without requiring reversals of the pulsing direction. For our choice of ω_{p0} , $b_1 + b_2 = 0.88$ ensures that the instantaneous precession frequency of the ^{131}Xe never goes below 1 Hz. The moving average filter most strongly attenuates frequency content at integer multiples of ω_3/N (where ω_3 sets the sampling rate). Since ρ was within 0.05% of $27/8$, we used the moving average filter to suppress residuals of the demodulation at ω_d^a , $\omega_1 = \omega_d^b$, and ω_2 by setting $\omega_d^a = \omega_3/6$ and $N = 27 \times \omega_3/\omega_d^a = 162$.

For ^{131}Xe we measure $b_b^S K_1^b \approx 30 \mu\text{G}$ or 0.1% polarization and a linewidth of $21.2(3)$ mHz. For ^{129}Xe we measure $b_a^S K_1^a \approx 10 \mu\text{G}$ or 0.3% polarization and a linewidth of $15.6(3)$ mHz. From Eq. 12 and estimates similar to Ref. [2], we anticipate polarizations of 0.05% for ^{131}Xe and 0.2% for ^{129}Xe .

The measured ^{129}Xe polarization is substantially lower than if it were limited only by relaxation due to SE collisions. A possible explanation for this discrepancy is an anomalous temperature-dependent wall relaxation mechanism similar to what has been reported in Rb- ^3He cells [34]. We fit the Xe-Rb polarization ratio as a func-

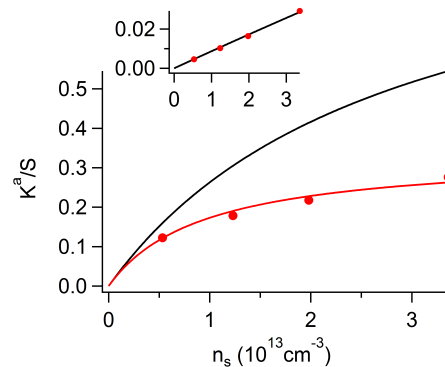


FIG. 5: Ratio of Xe to Rb polarization vs Rb density. Inset depicts K^b/S . Filled circles are measured data.

Black lines are theoretical curves which lack temperature-dependent wall relaxation. Red line is a fit of K^a/S vs Rb density which includes an anomalous wall relaxation free parameter.

tion of Rb density n_S with

$$\frac{K_\perp}{S_\perp} = \frac{\Gamma_S^K}{\Gamma_1} = \frac{\kappa_S^K n_S}{\kappa_S^K n_S (1+x) + \Gamma_{W0}}, \quad (17)$$

where κ_S^K is the SE rate coefficient, and the wall relaxation is $\Gamma_W = \Gamma_{W0} + x\Gamma_S^K$ with room-temperature relaxation Γ_{W0} . The x parameterizes the temperature dependence. Figure 5 shows the diminishing gains in ^{129}Xe polarization as the Rb density is increased, corresponding to $x = 2.0(1)$ in our cell. Previous measurement of a nominally spherical 8 mm cell (32 Torr ^{129}Xe , 8 Torr ^{131}Xe , 300 Torr N_2 , and ^{85}Rb) gave $x = 3.4$ for ^{129}Xe [29]. ^{131}Xe does not exhibit such a temperature-dependent effect; its polarization scales linearly with Rb density (see inset of Fig. 5). As this is a surface effect, it is likely related to the Rb hydride coating of our vapor cell. Further study is needed to understand the exact mechanism behind x . Such study will require measurements of vapor cells of various compositions and geometries.

Free induction decay studies suggest the presence of ≈ 30 mHz of first order quadrupole produced by the cell asymmetry caused by the cell's pull-off stem [35]. However, the measured ^{131}Xe signal exhibits no sign of quadrupole beating [6, 36] when excited via synchronous SEOP. Furthermore, the average (over many data sets) of the ratio of Xe resonance frequencies is 3.3727. Supposing that the discrepancy between the measured ratio of gyro-magnetic ratios and that reported in Ref. [28] is due solely to quadrupole, the quadrupole shift would be about 2 mHz. We believe the suppression of first order quadrupole is generic to transverse polarization and plan to explore this interesting observation in future work.

III. COMAGNETOMETRY

Simultaneous measurements of the Xe resonance frequencies Ω^a and Ω^b are required for the computation of the comagnetometer signal ξ . In our system, we measure the resonance frequencies using feedback. The phase δ of the Xe transverse polarization is much more sensitive to small fluctuations (or rotations) about the bias field than the magnitude K_{\perp} , and is therefore a useful error signal for feedback. Performing a Fourier transform of Eq. 14 gives

$$\tilde{\delta} = -\frac{\tilde{\Delta} \mp \Gamma_2 \tilde{\epsilon}_z}{i\omega + \Gamma_2}. \quad (18)$$

We stabilize the drive frequency of each isotope by servoing [37] the detected phase $\tilde{\delta} \mp \tilde{\epsilon}_z$. Doing so reduces uncertainty in the transformation from phase to frequency for each isotope. The feedback can be written

$$\tilde{\omega}_d = (\tilde{\delta} \mp \tilde{\epsilon}_z) \tilde{G}, \quad (19)$$

where \tilde{G} is the frequency dependent feedback gain (units of 2π Hz/rad). The finite gain corrected drive frequencies are then

$$\tilde{\omega}_d = \tilde{\omega}_d \tilde{G}^{-1} (i\omega + \Gamma_2 + \tilde{G}) = \tilde{\Omega}_0 \mp i\omega \tilde{\epsilon}_z. \quad (20)$$

The comagnetometer signal ξ' is computed as

$$\tilde{\xi}' \equiv \frac{\rho \tilde{\omega}_d^b - \tilde{\omega}_d^a}{1 + \rho} = \tilde{\xi} + i\omega \tilde{\epsilon}_z, \quad (21)$$

where $\omega^a, \omega^b > 0$. We see that the derivative of ϵ_z appears just like a rotation would in ξ' .

To extract ξ from ξ' , we need to know ϵ_z . We assumed that \tilde{B}_{z0} was the dominant contribution to $\tilde{\epsilon}_z$ and used the sum of the finite gain corrected drive frequencies, which should also be dominated by \tilde{B}_{z0} , to construct $\tilde{\epsilon}_z$ according to Eq. 9 as

$$\tilde{\epsilon}_z = \tan^{-1} \left(\frac{1}{B_w} \frac{\tilde{\omega}_d^a + \tilde{\omega}_d^b}{\gamma^a + \gamma^b} \right). \quad (22)$$

In the sections that follow we demonstrate the field suppression and stability of the comagnetometer. We will show that $\tilde{\epsilon}_z$ has a profound impact on the field suppression.

A. Field suppression

Each isotope is phase locked to line center with an accuracy of ± 0.3 mHz. The drive frequency of each isotope then tracks the resonance as defined by the phase of precession as measured by the Rb. These drive frequencies are recorded and corrected for finite gain (Eq. 20) in post-processing. The quantities $\tilde{\epsilon}_z$ and $\tilde{\xi}$ are also computed in post-processing (Eq. 21 and 22).

Figure 6 (a) shows the amplitude spectral densities of the drive frequencies and ξ . The spectrum of the ^{129}Xe

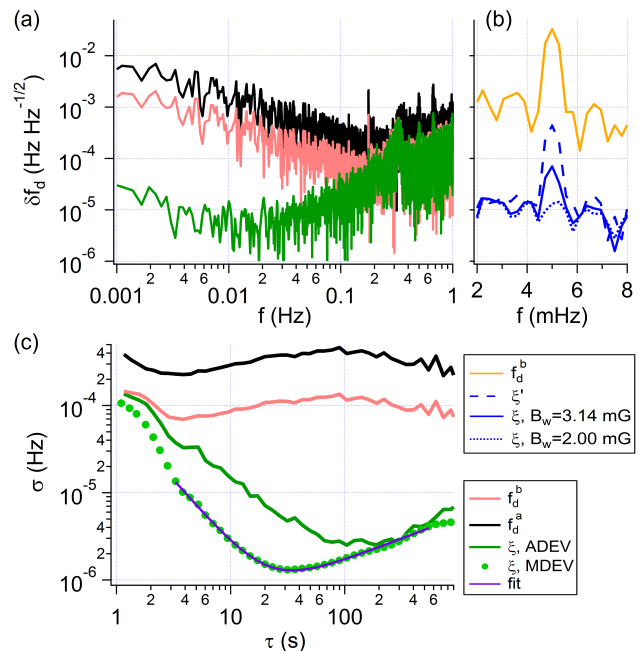


FIG. 6: (a) Amplitude spectral densities of $f_d^b = \omega_d^b/2\pi$, f_d^a , ξ . (b) Spectra with ancillary AC B_z applied showing the field suppression factor for various comagnetometer signal computations. (c) Allan Deviations of f_d^b , f_d^a , ξ , where ξ was analyzed with both standard and modified Allan deviations. All data shown have been corrected for finite gain. A Hanning window is applied to each spectrum.

drive frequency is very nearly ρ larger than the ^{131}Xe drive frequency spectrum from DC to 0.1 Hz, suggesting that \tilde{B}_{z0} dominates over this frequency band.

Since the goal of a comagnetometer is to sense non-magnetic spin-dependent interactions, we characterize how well the device rejects bias magnetic field perturbations. In order to characterize the field suppression factor (FSF) of the comagnetometer, we record the drive frequencies while applying an ancillary 5 mHz $4.3 \mu\text{G}$ B_z . We define the FSF to be $\tilde{\omega}_d^b/\tilde{\xi}'$ at the frequency of the ancillary B_z .

If we compute ξ using the average of two independent measurements of B_w (see next section) we find an FSF of 470. However, the maximum value of FSF occurs for $B_w = 2.0$ mG and is 2300. Ignoring the influence of ϵ_z and computing the FSF as $\tilde{\omega}_d^b/\tilde{\xi}'$ produces an FSF of merely 75. Clearly, ϵ_z introduces substantial phase shifts to the comagnetometer signal. In the following section we describe two independent measurements of B_w . We also describe a means of measuring the FSF without ambiguity introduced by uncertainty in B_w .

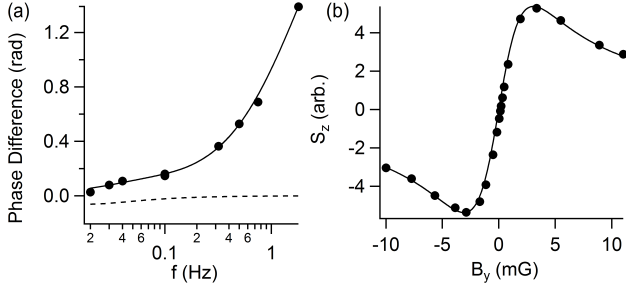


FIG. 7: (a) Open loop Xe phase difference. Dashed line is the calculated phase difference for $\tilde{\epsilon}_z = 0$. Line is a fit that includes ϵ_z . (b) Magnetometer response to B_y . Circles are measured data. Line is a dispersive fit to the data.

1. B_w measurements

We measure B_w independently using two methods. First, we measure the difference in open loop response (see Eq. 18) of the two Xe isotopes, which for $\omega \gg \Gamma_2$ and $\Delta^a = \Delta^b = 0$ is dominated by ϵ_z . The data in Fig. 7 (a) were acquired by setting ω_d to resonance for each isotope by hand (no ω_d feedback), applying an AC few μG B_{z0} at various frequencies, and recording the phase difference between the phase response of the two isotopes. Since we measure $\tilde{\delta} \mp \tilde{\epsilon}_z$ (as per Eq. 16), we construct a fit function

$$\begin{aligned} & \text{Arg}(\tilde{\delta}^a - \tilde{\epsilon}_z) - \text{Arg}(\tilde{\delta}^b + \tilde{\epsilon}_z) \\ & \approx \tan^{-1} \left(\frac{\omega(B_w \gamma^a - \Gamma_2^a)}{-\omega^2 - B_w \gamma^a \Gamma_2^a} \right) - \tan^{-1} \left(\frac{\omega(B_w \gamma^b + \Gamma_2^b)}{\omega^2 - B_w \gamma^b \Gamma_2^b} \right), \end{aligned} \quad (23)$$

where we have taken $\tilde{\Delta} \approx \gamma \tilde{B}_{z0}$ and $\tilde{\epsilon}_z \approx \tilde{B}_{z0}/B_w$. Using this fit function, we find $B_w = 3.5 \pm 0.3$ mG. If there were no magnetometer phase shift (i.e., if $\tilde{\epsilon}_z = 0$) the phase difference would approach zero with increasing frequency (see dashed line in Fig. 7). Instead we see the phase difference increase, consistent with our model for ϵ_z .

We can also obtain B_w by measuring the magnetometer response (without substantial Xe excitation) to a known B_y of various magnitudes, as shown in Fig. 7 (b). Fitting according to the \hat{z} component of Eq. 6, we find $B_w = 3.1 \pm 0.1$ mG. The weighted mean of the two measurements is $B_w = 3.14$ mG.

2. Stabilizing the sum frequency

In order to prevent uncertainty in B_w from influencing the FSF, we built an additional feedback loop which corrected B_{z0} such that the sum $\omega_d^a + \omega_d^b$ was kept fixed. Assuming that B_{z0} is the dominant contribution to ϵ_z , this will stabilize the magnetometer phase shift. The gain of this feedback loop was sufficient to suppress $\tilde{\omega}_d^b$

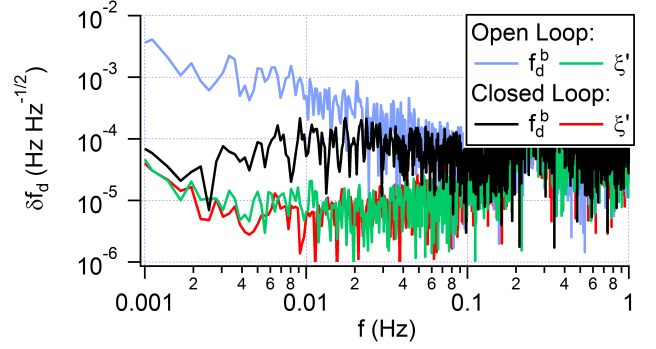


FIG. 8: Influence of stabilizing $\omega_d^a + \omega_d^b$ on \tilde{f}_d^b and $\tilde{\xi}^i$. Open loop data are without stabilization. Closed loop data are with stabilization.

by a factor of 15 at 5 mHz compared to when the sum $\omega_d^a + \omega_d^b$ was not stabilized, as shown in Fig. 8. The FSF was 1800 with this additional feedback loop (taking into account the factor of 15 suppression of $\tilde{\omega}_d^b$).

The low-frequency FSF of other comagnetometer implementations are often not reported in the literature. The K- ^{21}Ne comagnetometer from Ref. [3] reports an FSF starting at 10^3 at 1 Hz and decreasing linearly with applied B_z frequency. Extrapolating to 5 mHz suggests an FSF of $\approx 10^4$ at 5 mHz, an order of magnitude greater than that which we demonstrate in this paper.

In the next section we demonstrate the stability of our comagnetometer. In particular we show that the stability is not limited by residual bias field fluctuations and/or finite FSF.

B. Stability

Without an ancillary B_z , ξ 's amplitude spectral density (see Fig. 6) has a distinct f trending noise from 1 to 0.02 Hz until it reaches a white noise level of $< 10 \mu\text{Hz}/\sqrt{\text{Hz}}$. Both the f trending and white frequency noises are due to finite SNR and are discussed below. We find that the noise of ξ is the same regardless of the B_w used in computation and whether or not we stabilize B_{z0} using the sum of the drive frequencies (both $\tilde{\xi}^i$ in Fig. 8 are similar). This suggests that ξ 's noise is not limited by the FSF. A B_w of 3.14 mG was used for the ξ shown in Fig. 6 (a) and (c).

Figure 6 (c) shows the standard Allan deviation (ADEV) of the drive frequencies and the comagnetometer signal ξ . It also depicts the modified Allan deviation (MDEV) [38, 39] of ξ . The ADEV of the drive frequencies are mostly constant with τ suggesting that they are dominated by flicker frequency noise. The high level of correlation between the two drive frequencies allows for a ξ whose deviation is orders of magnitude smaller. The deviation of ξ is dominated by white phase noise from 1 to 30 seconds of integration (as indicated by the $\tau^{-3/2}$ slope of the MDEV) and random walk of frequency from

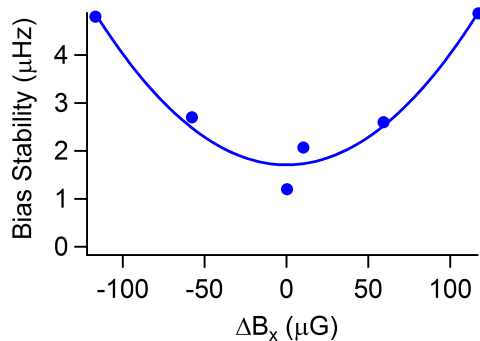


FIG. 9: Bias instability dependence on DC B_x . Line is a quadratic fit to the data.

30 seconds onward.

We fit the MDEV from Fig. 6 (c) using the function $\sigma^2 = (a\tau^{-3/2})^2 + (b\tau^{-1/2})^2 + (c\tau^{1/2})^2$ and find $a = 78.2(7)$ $\mu\text{Hz Hz}^{-3/2}$, $b = 4.3(4)$ $\mu\text{Hz Hz}^{-1/2}$, and $c = 168(3)$ $\text{nHz Hz}^{1/2}$. The angle-random walk (ARW) is $b\sqrt{2}$ or $6.1(4)$ $\mu\text{Hz}/\sqrt{\text{Hz}}$.

We can estimate how finite SNR influences the comagnetometer stability by re-writing the comagnetometer signal to explicitly include the noise \tilde{n} (SNR^{-1}) of our detection such that the measured phase of each isotope is $\tilde{\delta} \mp \tilde{\epsilon}_z + \tilde{n}$. The expression for $\tilde{\xi}^t$ (see Eq. 21) including the uncorrelated noise \tilde{n} for each noble gas species becomes

$$\tilde{\xi}^t = \tilde{\xi} + i\omega\tilde{\epsilon}_z + \frac{\rho(i\omega + \Gamma_2^b)\tilde{n}^b - (i\omega + \Gamma_2^a)\tilde{n}^a}{1 + \rho}. \quad (24)$$

If $\tilde{\xi}$ is dominated by \tilde{n} then $\tilde{\xi}$ will have a white noise spectrum which changes to f trending noise near $\omega \approx \Gamma_2$.

The white phase noise level measured under open loop conditions suggest SNRs of $5300 \sqrt{\text{Hz}}$ and $3200 \sqrt{\text{Hz}}$ for ^{131}Xe and ^{129}Xe , respectively. The SNR-limited ARW calculated from Eq. 24 is $4 \mu\text{Hz}/\sqrt{\text{Hz}}$, which is very similar to the ARW found by fitting the MDEV of ξ . The photon shot noise limited ARW is $10 \text{ nHz}/\sqrt{\text{Hz}}$. It is unclear what is presently limiting the SNR. We have confirmed that our detection noise is not limited by probe technical noise. It may be that our demodulation routine introduces noise. We may also be limited by finite bias pulse repetition rate modulation fidelity (drive-to-noise ratio). These are topics for future study.

It is uncertain what limits the bias instability. We find that the measured bias instability is most sensitive to a DC B_x , as shown in Fig. 9, which suggests that $1/f$ B_x field fluctuations may be an important contributor to bias instability. We believe the mechanism for this dependence is related to imperfect cancellation of the Rb SE field, which depends critically on pump laser detuning, Rb density, and DC B_x . When the Rb SE field is not well cancelled, K_z (a known source of systematic error) will be produced if $\Delta \neq 0$. We plan to study this effect in the near future.

IV. OUTLOOK

The accuracy of the device can be quantified by making measurements of a known non-magnetic spin-dependent phenomenon, such as Earth's rotation rate. This can be accomplished by orienting the sensitive axis of the comagnetometer parallel to Earth's axis of rotation. The demonstrated comagnetometer performance should allow resolution of Earth's rotation rate after less than 10 seconds of integration.

Further increase in comagnetometer sense bandwidth (beyond the 1 Hz bandwidth demonstrated here) is desirable for inertial navigation applications. The fundamental sense bandwidth of the comagnetometer is limited by ω_2 , which in this work was ≈ 3.7 Hz. The value of ω_2 can be increased by increasing the average pulse repetition rate of the bias pulses or increasing their area to produce $2\pi m$ Larmor rotation of the Rb, where m is an integer greater than one. However, in order to sample the ^{129}Xe precession without violating Nyquist's criterion, the gating frequency ω_3 (see Eq. 5) must be at least twice that of the average ^{129}Xe precession frequency. The gating frequency is limited by the Rb magnetometer response. The magnetometer response can be increased via feedback by applying AC B_y fields to cancel the Xe SE fields experienced by the Rb so that the Rb is kept at zero field.

The performance of synchronous SE comagnetometry applied to ^3He - ^{129}Xe cells looks very promising. Compared to ^{131}Xe - ^{129}Xe , a ^3He - ^{129}Xe cell should enable roughly 10 times the T_2 and 10 times the signal [1, 40]. If the modest magnetic sensitivity remained the same as our current cell then the anticipated ARW would be $100 \text{ nHz}/\sqrt{\text{Hz}}$, an order of magnitude less than what was reported in Ref. [1]. Although the improvement in SNR should be dramatic, the sensitivity to longitudinal Rb fields will be much larger ($b_S^a = 110b_S^{\text{He}}$ [41] versus $b_S^a = 1.002b_S^b$ [6, 22]), as will the sensitivity to first-order temperature gradients [42] and back polarization [1].

The through-space J-coupling term b_a^b depends on cell geometry and the frequency enhancement factor κ_a^b which has yet to be measured but was recently calculated to be 0.3 [20, 43]. We estimate that for our apparatus $K_z^a = 0.1K_{max}^a$ would produce a comagnetometer frequency shift of a few μHz , which would be well resolved by this device.

Dual-species synchronous SEOP is an excellent technique for performing a direct search for axion-induced spin-mass couplings. Because of the Yukawa type potentials assumed for spin-mass couplings, miniaturized comagnetometers enable broad energy resolution of the supposed coupling. If the results reported in this study are reproduced in a 2 mm cell [6], we anticipate being able to improve the present upper bound in the submillimeter wavelength range by an order of magnitude.

V. CONCLUSION

We have demonstrated the first SE pumped comagnetometer which continuously polarizes alkali-metal atoms and noble gas nuclei in a purely transverse manner. The pure transverse polarization suppresses the influence of K_z and S_z on the comagnetometer signal. The application of the bias field as a sequence of low duty cycle pulses whose area correspond to 2π precession of the alkali-metal atoms enables magnetic field modulations which are experienced by the noble gas and not by the alkali-metal atoms.

The embedded alkali-metal magnetometer was used to detect the precession phase of two noble gas isotopes simultaneously with a sample rate of 200 Hz. The measured ^{129}Xe polarization appears to be limited by a temperature-dependent wall relaxation mechanism. This effect is independent of the continuous excitation method described in this work and likely stems from the cell's Rb hydride coating. The comagnetometer was operated in a closed loop fashion such that the drive frequencies of each isotope were corrected to keep their measured phases equal to zero. The closed loop noble gas precession frequencies were shown to be sufficiently well correlated to enable a field suppression factor of 10^3 , which was more than sufficient to suppress the low frequency field noise such that the white noise of the device was apparent. Our system has a 1 Hz measurement bandwidth, and the ARW was found to be $7 \mu\text{Hz} / \sqrt{\text{Hz}}$, within a factor of two of the SNR limit. To first order, the comagnetome-

ter scale factor can be written in terms of fundamental constants.

We have demonstrated dramatic improvement of the field suppression factor when accounting for the phase of the alkali-metal magnetometer. This is accomplished by computing ϵ_z from the stray field noise in B_z (which we determine from the sum of the recorded Xe drive frequencies) and including it in the computation of the comagnetometer signal. A similar field suppression factor was achieved by stabilizing the stray field in real time. While our calculations assumed ϵ_z was dominated by B_z , other possible contributions include K_z , pump pointing, and back polarization (K_y producing S_y). We could monitor ϵ_z directly by applying an ancillary rotating B_\perp and measuring the response of the magnetometer, allowing for improved suppression of the magnetometer phase shift in the comagnetometry.

ACKNOWLEDGMENTS

We acknowledge Anna Korver and Josh Weber for prior supporting work, and Michael Bulatowicz for his help in designing the pulse driver circuit. We would like to thank Michael Larsen for insightful discussions. This research was supported by the National Science Foundation (PHY-1607439 and PHY-1912543) and Northrop Grumman Mission Systems' University Research Program.

-
- [1] M. E. Limes, D. Sheng, and M. V. Romalis, “ ^3He - ^{129}Xe comagnetometry using ^{87}Rb detection and decoupling,” *Phys. Rev. Lett.* **120**, 033401 (2018).
 - [2] T.G. Walker and M.S. Larsen, “Spin-exchange-pumped nmr gyros,” *Advances In Atomic, Molecular, and Optical Physics*, **65**, 373 – 401 (2016).
 - [3] T. W. Kornack, R. K. Ghosh, and M. V. Romalis, “Nuclear spin gyroscope based on an atomic comagnetometer,” *Physical review letters* **95**, 230801 (2005).
 - [4] Liwei Jiang, Wei Quan, Rujie Li, Wenfeng Fan, Feng Liu, Jie Qin, Shuangai Wan, and Jiancheng Fang, “A parametrically modulated dual-axis atomic spin gyroscope,” *Applied Physics Letters* **112**, 054103 (2018), <https://doi.org/10.1063/1.5018015>.
 - [5] F. A. Karwacki, “Nuclear magnetic resonance gyro development,” *Navigation* **27**, 72 (1980).
 - [6] M. Bulatowicz, R. Griffith, M. Larsen, J. Mirijanian, C. B. Fu, E. Smith, W. M. Snow, H. Yan, and T. G. Walker, “Laboratory search for a long-range T -odd, P -odd interaction from axionlike particles using dual-species nuclear magnetic resonance with polarized ^{129}Xe and ^{131}Xe gas,” *Phys. Rev. Lett.* **111**, 102001 (2013).
 - [7] J. Lee, A. Almasi, and M. V. Romalis, “Improved limits on spin-mass interactions,” *Phys. Rev. Lett.* **120**, 161801 (2018).
 - [8] F. Allmendinger, W. Heil, S. Karpuk, W. Kilian, A. Scharth, U. Schmidt, A. Schnabel, Yu. Sobolev, and K. Tullney, “New limit on lorentz-invariance- and CPT -violating neutron spin interactions using a free-spin-precession ^3He - ^{129}Xe comagnetometer,” *Phys. Rev. Lett.* **112**, 110801 (2014).
 - [9] M. V. Romalis, D. Sheng, B. Saam, and T. G. Walker, “Comment on “new limit on lorentz-invariance- and CPT -violating neutron spin interactions using a free-spin-precession ^3He - ^{129}Xe comagnetometer,”” *Phys. Rev. Lett.* **113**, 188901 (2014).
 - [10] M. Smiciklas, J. M. Brown, L. W. Cheuk, S. J. Smullin, and M. V. Romalis, “New test of local lorentz invariance using a ^{21}Ne -Rb-K comagnetometer,” *Phys. Rev. Lett.* **107**, 171604 (2011).
 - [11] J. M. Brown, S. J. Smullin, T. W. Kornack, and M. V. Romalis, “New limit on lorentz- and CPT -violating neutron spin interactions,” *Phys. Rev. Lett.* **105**, 151604 (2010).
 - [12] A. G. Glenday, C. E. Cramer, D. F. Phillips, and R. L. Walsworth, “Limits on anomalous spin-spin couplings between neutrons,” *Phys. Rev. Lett.* **101**, 261801 (2008).
 - [13] M. A. Rosenberry and T. E. Chupp, “Atomic electric dipole moment measurement using spin exchange pumped masers of ^{129}Xe and ^3He ,” *Phys. Rev. Lett.* **86**, 22–25 (2001).
 - [14] F. Allmendinger, I. Engin, W. Heil, S. Karpuk, H.-J.

- Krause, B. Niederländer, A. Offenhäusser, M. Repetto, U. Schmidt, and S. Zimmer, “Measurement of the permanent electric dipole moment of the ^{129}Xe atom,” *Phys. Rev. A* **100**, 022505 (2019).
- [15] N. Sachdeva, I. Fan, E. Babcock, M. Burghoff, T. E. Chupp, S. Degenkolb, P. Fierlinger, S. Haude, E. Kraegeloh, W. Kilian, S. Knappe-Grüneberg, F. Kuchler, T. Liu, M. Marino, J. Meinel, K. Rolfs, Z. Salhi, A. Schnabel, J. T. Singh, S. Stuibler, W. A. Terrano, L. Trahms, and J. Voigt, “New limit on the permanent electric dipole moment of ^{129}Xe using ^3He comagnetometry and squid detection,” *Phys. Rev. Lett.* **123**, 143003 (2019).
- [16] C. H. Volk, T.M. Kwon, and J. G. Mark, “Measurement of the ^{87}Rb – ^{129}Xe spin-exchange cross section,” *Phys. Rev. A* **21**, 1549–1555 (1980).
- [17] T. M. Kwon, J. G. Mark, and C. H. Volk, “Quadrupole nuclear spin relaxation of ^{131}Xe in the presence of rubidium vapor,” *Phys. Rev. A* **24**, 1894–1903 (1981).
- [18] E.A. Donley, “Nuclear magnetic resonance gyroscopes,” in *Sensors, 2010 IEEE* (2010) pp. 17–22.
- [19] T.G. Walker and W. Happer, “Spin-exchange optical pumping of noble-gas nuclei,” *Rev. Mod. Phys.* **69**, 629–642 (1997).
- [20] M. E. Limes, N. Dural, M. V. Romalis, E. L. Foley, T. W. Kornack, A. Nelson, L. R. Grisham, and J. Vaara, “Dipolar and scalar ^3He – ^{129}Xe frequency shifts in stemless cells,” *Phys. Rev. A* **100**, 010501(R) (2019).
- [21] W. A. Terrano, J. Meinel, N. Sachdeva, T. E. Chupp, S. Degenkolb, P. Fierlinger, F. Kuchler, and J. T. Singh, “Frequency shifts in noble-gas comagnetometers,” *Phys. Rev. A* **100**, 012502 (2019).
- [22] V. I. Petrov, A. S. Pazgalev, and A. K. Vershovskii, “Isotope shift of nuclear magnetic resonances in ^{129}Xe and ^{131}Xe caused by spin-exchange pumping by alkali metal atoms,” *IEEE Sensors Journal*, 1–1 (2019).
- [23] S. R. Schaefer, G. D. Cates, Ting-Ray Chien, D. Gonatas, W. Happer, and T. G. Walker, “Frequency shifts of the magnetic-resonance spectrum of mixtures of nuclear spin-polarized noble gases and vapors of spin-polarized alkali-metal atoms,” *Phys. Rev. A* **39**, 5613–5623 (1989).
- [24] T. E. Chupp, E. R. Oteiza, J. M. Richardson, and T. R. White, “Precision frequency measurements with polarized ^3He , ^{21}Ne , and ^{129}Xe atoms,” *Phys. Rev. A* **38**, 3998–4003 (1988).
- [25] Y. Takahashi, K. Honda, N. Tanaka, K. Toyoda, K. Ishikawa, and T. Yabuzaki, “Quantum nondemolition measurement of spin via the paramagnetic faraday rotation,” *Phys. Rev. A* **60**, 4974–4979 (1999).
- [26] O. Katz, R. Shaham, and O. Firstenberg, “Quantum interface for noble-gas spins,” (2019), arXiv:1905.12532 [quant-ph].
- [27] A. I. Nahlawi, Z. L. Ma, M. S. Conradi, and B. Saam, “High-precision determination of the frequency-shift enhancement factor in Rb – ^{129}Xe ,” *Phys. Rev. A* **100**, 053415 (2019).
- [28] W. Makulski, “ ^{129}Xe and ^{131}Xe nuclear magnetic dipole moments from gas phase nmr spectra,” *Magnetic Resonance in Chemistry* **53**, 273–279 (2015), <https://onlinelibrary.wiley.com/doi/pdf/10.1002/mrc.4191>.
- [29] A. Korver, D. Thrasher, M. Bulatowicz, and T. G. Walker, “Synchronous spin-exchange optical pumping,” *Phys. Rev. Lett.* **115**, 253001 (2015).
- [30] D. A. Thrasher, S. S. Sorensen, J. Weber, M. Bulatowicz, A. Korver, M. Larsen, and T. G. Walker, “Continuous comagnetometry using transversely polarized xe isotopes,” *Phys. Rev. A* **100**, 061403(R) (2019).
- [31] D. Brinkmann, E. Brun, and H. H. Staub, “Kernresonanz im gasförmigen xenon,” *Helv. Phys. Acta* **35**, 431 (1962).
- [32] A. Korver, R. Wyllie, B. Lancor, and T. G. Walker, “Suppression of spin-exchange relaxation using pulsed parametric resonance,” *Phys. Rev. Lett.* **111**, 043002 (2013).
- [33] N. D. Bhaskar, M. Hou, M. Ligare, B. Suleman, and W. Happer, “Role of Na-Xe molecules in spin relaxation of optically pumped Na in Xe gas,” *Phys. Rev. A* **22**, 2710–2716 (1980).
- [34] E. Babcock, B. Chann, T. G. Walker, W. C. Chen, and T. R. Gentile, “Limits to the polarization for spin-exchange optical pumping of ^3He ,” *Phys. Rev. Lett.* **96**, 083003 (2006).
- [35] Z. Wu, S. Schaefer, G. D. Cates, and W. Happer, “Coherent interactions of the polarized nuclear spins of gaseous atoms with the container walls,” *Phys. Rev. A* **37**, 1161–1175 (1988).
- [36] E. A. Donley, J. L. Long, T. C. Liebisch, E. R. Hodby, T. A. Fisher, and J. Kitching, “Nuclear quadrupole resonances in compact vapor cells: The crossover between the nmr and the nuclear quadrupole resonance interaction regimes,” *Phys. Rev. A* **79**, 013420 (2009).
- [37] J. Bechhoefer, “Feedback for physicists: A tutorial essay on control,” *Rev. Mod. Phys.* **77**, 783–836 (2005).
- [38] D.W. Allan and J.A. Barnes, “A modified "allan variance" with increased oscillator characterization ability,” *Proceedings of the 35th Annual Frequency Control Symposium, Philadelphia, 1981*, 470–475.
- [39] J. Vanier and C. Audoin, in *The Quantum Physics of Atomic Frequency Standards*, Vol. 1 (IOP Publishing Ltd, Bristol, 1989) Chap. Appendix 2F, pp. 216–256.
- [40] T. R. Gentile, P. J. Nacher, B. Saam, and T. G. Walker, “Optically polarized ^3He ,” *Rev. Mod. Phys.* **89**, 045004 (2017).
- [41] Z. L. Ma, E. G. Sorte, and B. Saam, “Collisional ^3He and ^{129}Xe frequency shifts in rb–noble-gas mixtures,” *Phys. Rev. Lett.* **106**, 193005 (2011).
- [42] D. Sheng, A. Kabcenell, and M. V. Romalis, “New classes of systematic effects in gas spin comagnetometers,” *Phys. Rev. Lett.* **113**, 163002 (2014).
- [43] J. Vaara and M. V. Romalis, “Calculation of scalar nuclear spin-spin coupling in a noble-gas mixture,” *Phys. Rev. A* **99**, 060501(R) (2019).